

Cubic Spline Collocation Method for the Shallow Water Equations on the Sphere

Anita T. Layton¹

*National Center for Atmospheric Research, Advanced Study Program, 1850 Table
Mesa Drive, Boulder, Colorado 80303
E-mail: layton@amath.unc.edu*

Received July 16, 2001; revised March 29, 2002

Spatial discretization schemes commonly used in global meteorological applications are currently limited to spectral methods or low-order finite-difference/finite-element methods. The spectral transform method, which yields high-order approximations, requires Legendre transforms, which have a computational complexity of $\mathcal{O}(N^3)$, where N is the number of subintervals in one dimension. Thus, high-order finite-element methods may be a viable alternative to spectral methods. In this study, we present a new numerical method for solving the shallow water equations (SWE) in spherical coordinates. In this implementation, the SWE are discretized in time with the semi-implicit leapfrog method, and in space with the cubic spline collocation method on a skipped latitude–longitude grid. Numerical results for the Williamson *et al.* SWE test cases [D. L. Williamson, J. B. Blake, J. J. Hack, R. Jakob, and P. N. Swarztrauber, *J. Comput. Phys.* **102**, 211 (1992)] are presented to demonstrate the stability and accuracy of the method. Results are also shown for an efficiency comparison between this method and a similar method in which spatial discretization is done on a uniform latitude–longitude grid. © 2002 Elsevier Science (USA)

Key Words: shallow water equations; cubic splines; collocation methods; numerical weather prediction; finite element; leapfrog scheme; semi-implicit scheme; spherical coordinates.

1. INTRODUCTION

Climate modeling, which predicts statistical meteorological quantities, is important, as it helps us understand, for example, the mechanisms of atmospheric and oceanic circulations, as well as the effects of technological advancements on the atmosphere. The importance of weather-prediction is well understood, as weather affects us in a multitude of ways through

¹ Present address: Department of Mathematics, University of North Carolina, Chapel Hill, NC 27599.

agriculture, recreation, and transportation. The accuracy of climate and weather prediction depends on many factors, among which are the accuracy of the knowledge of the state of the atmosphere at initial time, the numerical methods applied, and the resolution used in the methods. Because computational atmospheric problems are known to be very time-consuming, there is a lot of interest among the scientific community in studying accurate and efficient methods for these problems. One way to achieve high accuracy in climate- and weather-prediction computations is to use high-order discretization methods.

Spatial discretization schemes that are commonly used in global meteorological simulations are spectral schemes, finite-difference schemes, and finite-element schemes. Currently there is some controversy over which of the three approaches is preferable for the integration of weather models. For instance, models at the National Center for Atmospheric Research (NCAR) and the European Center for Medium-Range Weather Forecasts (ECMWF) incorporate the spectral transform method [11, 21], whereas a model developed by the Canadian Meteorological Centre in partnership with the Meteorological Research Branch (CMC-MRB) adopts a variable-resolution cell-integrated finite-element scheme [1, 2].

The spectral transform method represents the solution of a problem in spherical coordinates in terms of spherical harmonics. Since spherical harmonics are the natural representation of the solution of a two-dimensional problem on the sphere, the spectral transform method provides a natural solution to a technical aspect of the *pole problem*, which is that some variables (e.g., the longitudinal and latitudinal wind images) may not be well defined at the poles. Also, since the spherical harmonics are eigenfunctions of the Laplacian on the sphere, the semi-implicit Helmholtz problem is relatively trivial to solve in spectral space. Another advantage of the spectral transform method is that, provided the solution is sufficiently smooth, the method generates numerical approximations with exponential convergence and thus with accuracy higher than most other methods (e.g., finite-difference methods) for sufficiently high spatial resolutions.

Although the spectral transform method seems ideal for the spherical domain, it also has some disadvantages. Provided that an optimal solver is applied for the solution of the linear system arising from the Helmholtz problem, the computational cost of finite-difference and finite-element methods applied to the shallow water equations (SWE) on the sphere increases quadratically with the number of grid points in one dimension (i.e., $\mathcal{O}(N^2)$, where N is the number of spatial subintervals in one dimension). However, the cost of performing spectral transforms increases more rapidly. In the case of Fourier transforms in the longitudinal direction, fast Fourier transforms (FFTs) may be used and their computational cost grows as $\mathcal{O}(N^2 \log(N))$. An efficient method for performing Legendre transforms, analogous to FFTs, has not yet been developed. Thus, the Legendre transforms in the latitudinal direction are often performed by summation and their costs escalate at a rate of $\mathcal{O}(N^3)$. Moreover, the spectral method is formally equivalent to a least-squares approximation that minimizes the mean square error over the global domain. This implies that the size of the error is likely to be the same everywhere. This may be a serious disadvantage in more comprehensive atmospheric models for a field, such as water vapor, for which the average value varies greatly over the globe. In the case of water vapor, for example, a small absolute error may be insignificant in equatorial regions, but it may completely alter the character of the field in polar regions [20]. Thus, there is interest in the atmospheric community in developing alternative high-order numerical methods.

In this study, we present a high-order finite-element spatial discretization method for the SWE in spherical coordinates. The SWE are discretized in time using the semi-implicit

leapfrog method, and in space using the cubic spline collocation method on a skipped latitude–longitude grid. The simplest numerical grid covering the entire sphere is the familiar latitude–longitude grid, but the convergence of meridians toward the poles necessitates special measures if such a grid is to be used for a numerical simulation of the atmosphere. When an Eulerian time integration method is used, time-step size is restricted by the Courant–Friedrichs–Lewy (CFL) condition and is determined essentially by the shortest resolvable scale divided by the largest phase speed of modes treated explicitly. Rather than allow the atypically high resolution near the poles to dictate time-step size, one may use a skipped grid in which the longitudinal increment $\Delta\lambda$ increases near the poles.

In Section 2, we construct a skipped grid and define bicubic spline basis functions. We then describe the procedures with which the SWE are discretized in time using the semi-implicit leapfrog scheme and in space using the cubic spline collocation method. In Section 3, we present numerical results for the Williamson *et al.* test suite for the SWE in spherical geometry [19] and we show that the method gives rise to stable numerical approximations that are third order near the poles and fourth order elsewhere. We also show that the method has a computational complexity of $\mathcal{O}(N^2)$ and we compare the efficiency of this method with that of a similar method with spatial discretization done on a uniform grid.

2. MODEL FORMULATION

The SWE, which describe the inviscid flow of a thin layer of fluid in two dimensions [10], have been used for many years by the atmospheric modeling community as a vehicle for testing promising numerical methods for solving atmospheric and oceanic problems. Because Earth is approximately spherical, most global atmospheric models in use today are based on spherical coordinates. To define the equations on the sphere, let u and v be the wind velocity components in the longitudinal and latitudinal directions, respectively, and ϕ be the geopotential perturbation from the mean geopotential ϕ^* , which is assumed to be constant. Let R be the radius of the earth, Ω be its rotational speed, and $f = 2\Omega \sin \theta$ be the Coriolis parameter, where R and Ω are assumed to be constant. In spherical coordinates, the SWE are given by

$$u_t + \frac{uu_\lambda}{R \cos \theta} + \frac{vu_\theta}{R} - \left(f + \frac{u \tan \theta}{R} \right) v + \frac{\phi_\lambda}{R \cos \theta} = 0, \quad (1)$$

$$v_t + \frac{uv_\lambda}{R \cos \theta} + \frac{vv_\theta}{R} + \left(f + \frac{u \tan \theta}{R} \right) u + \frac{\phi_\theta}{R} = 0, \quad (2)$$

$$\phi_t + \frac{u\phi_\lambda}{R \cos \theta} + \frac{v\phi_\theta}{R} + \frac{\phi + \phi^*}{R \cos \theta} (u_\lambda + (v \cos \theta)_\theta) = 0, \quad (3)$$

where the subscript denotes the partial derivative with respect to that variable. Since u and v are multivalued at the poles, we adopt the approach of Côté and Staniforth [4] and compute the components of the wind images instead: $U \equiv u \cos \theta / R$ and $V \equiv v \cos \theta / R$. Thus, expressing (1)–(3) in terms of U and V , we solve the equations

$$U_t + \frac{UU_\lambda}{\cos^2 \theta} + \frac{VV_\theta}{\cos \theta} - fV + \frac{\phi_\lambda}{R^2} = 0, \quad (4)$$

$$V_t + \frac{UV_\lambda}{\cos^2 \theta} + \frac{VV_\theta}{\cos \theta} + fU + \frac{\cos \theta}{R^2} \phi_\theta + \delta = 0, \quad (5)$$

$$\cos \theta \phi_t + \frac{U \phi_\lambda}{\cos \theta} + V \phi_\theta + (\phi + \phi^*) \left(\frac{U_\lambda}{\cos \theta} + V_\theta \right) = 0, \quad (6)$$

where $\delta \equiv (U^2 + V^2) \sin \theta / \cos^2 \theta$.

The geopotential is assumed to be periodic over the sphere; that is, ϕ is periodic along the longitude and along any two meridians associated with longitudes λ and $\lambda + \pi$. That is,

$$D_\lambda^{(k)} \phi(\lambda, \theta) = D_\lambda^{(k)} \phi(\lambda + 2\pi, \theta), \quad D_\theta^{(k)} \phi(\lambda, \pm\pi/2) = (-1)^k D_\theta^{(k)} \phi(\lambda + \pi, \pm\pi/2), \quad (7)$$

where k is a nonnegative integer and $D_s^{(k)}$ denotes the k th derivative operator with respect to the variable s . The wind images U and V are periodic along the longitude and satisfy the homogeneous Dirichlet boundary conditions at the poles. That is,

$$D_\lambda^{(k)} U(\lambda, \theta) = D_\lambda^{(k)} U(\lambda + 2\pi, \theta), \quad U(\lambda, \pm\pi/2) = 0. \quad (8)$$

The latitudinal wind image V satisfies similar conditions.

2.1. Cubic Splines on a Skipped Grid

The SWE are discretized in space using the cubic spline collocation method on a skipped grid. In this section, we construct the skipped grid and define two sets of bicubic spline basis functions that satisfy the boundary conditions (7) and (8), respectively.

On a uniform latitude–longitude grid, the meridians converge toward the poles and the physical distance between grid lines becomes small. Thus, as we show in Section 3.2, the time-step size required for a Eulerian method to maintain stability may become prohibitively restrictive owing to the CFL condition. Rather than allow the atypically high resolution near the poles to dictate the time-step size, one may use a grid in which the longitudinal increment $\Delta\lambda$ increases near the poles [7, 13, 16, 18]. Such a grid is commonly known as a skipped latitude–longitude grid. In [8], Göttemann solved the SWE using a linear spline collocation scheme on a skipped latitude–longitude grid and obtained second-order numerical approximations. In this study, we present a cubic spline collocation scheme for discretizing the SWE on a skipped grid, which is constructed similarly to that described in [8].

To define the skipped-grid partition, let k be a positive integer and $N_\theta = 2^k$ be the number of subintervals along the latitudinal dimension ($-\pi/2 \leq \theta \leq \pi/2$). The number of grid points along a latitude circle may decrease toward the poles. We define N_λ , the number of grid points along the j th latitude circle, to be

$$N_{\lambda_j} = \begin{cases} 0, & j = 0, N_\theta, \\ 2^{\lceil 1 + \log_2((N_\theta - j)\pi) \rceil}, & 0 < j < \frac{N_\theta}{4}, \\ 2^{\lceil 1 + \log_2(j\pi) \rceil}, & \frac{3N_\theta}{4} < j < N_\theta, \\ 2N_\theta, & \frac{N_\theta}{4} \leq j \leq \frac{3N_\theta}{4}, \end{cases} \quad (9)$$

where $j = 0, \dots, N_\theta$.

Let $\Delta\lambda_j = 2\pi/N_{\lambda_j}$ for $j = 0, \dots, N_\theta$, and $\Delta\theta = \pi/N_\theta$. Let $\lambda_i^{(j)} = i\Delta\lambda_j$ and $\theta_j = j\Delta\theta$. Then the skipped-grid partition is defined by $\mathcal{S} = \{(\lambda_i^{(j)}, \theta_j)\}$, for $i = 0, \dots, N_{\lambda_j} - 1$ and $j = 0, \dots, N_\theta$. The polar region of the skipped grid ($\pi/4 \leq \theta \leq \pi/2$) is shown in Fig. 1 for $N_\theta = 32$.

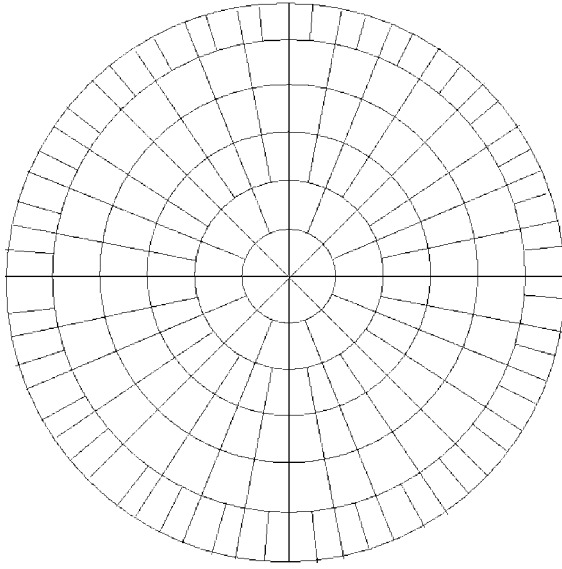


FIG. 1. The polar region of the skipped grid with $N_0 = 32$.

We now define the piecewise bicubic spline basis functions on \mathcal{S} . The model cubic spline function $\bar{\psi}$ in one dimension is defined by

$$\bar{\psi}(\lambda) = \begin{cases} \lambda^3, & 0 \leq \lambda \leq 1, \\ 1 + 3(\lambda - 1) + 3(\lambda - 1)^2 - 3(\lambda - 1)^3, & 1 < \lambda \leq 2, \\ 1 + 3(3 - \lambda) + 3(3 - \lambda)^2 - 3(3 - \lambda)^3, & 2 < \lambda \leq 3, \\ (4 - \lambda)^3, & 3 < \lambda \leq 4, \\ 0, & \text{otherwise.} \end{cases} \quad (10)$$

Let $\psi_i^{(j)}(\lambda) = \frac{1}{4}\bar{\psi}(\frac{\lambda}{\Delta\lambda_j} - i + 2)$. Define the one-dimensional periodic cubic basis functions along the j th latitude circle by

$$\beta_0^{(j)}(\lambda) = \begin{cases} \psi_0^{(j)}(\lambda), & \lambda \in [\lambda_0^{(j)}, \lambda_2^{(j)}], \\ \psi_{N_{\lambda_j}}^{(j)}(\lambda), & \lambda \in [\lambda_{N_{\lambda_j}-2}^{(j)}, \lambda_{N_{\lambda_j}}^{(j)}], \\ 0, & \text{otherwise,} \end{cases}$$

$$\beta_1^{(j)}(\lambda) = \begin{cases} \psi_1^{(j)}(\lambda), & \lambda \in [\lambda_0^{(j)}, \lambda_3^{(j)}], \\ \psi_{N_{\lambda_j}+1}^{(j)}(\lambda), & \lambda \in [\lambda_{N_{\lambda_j}-1}^{(j)}, \lambda_{N_{\lambda_j}}^{(j)}], \\ 0, & \text{otherwise,} \end{cases} \quad (11)$$

$$\beta_i^{(j)}(\lambda) = \psi_i^{(j)}(\lambda), \quad i = 2, \dots, N_{\lambda_j} - 2,$$

$$\beta_{N_{\lambda_j}-1}^{(j)}(\lambda) = \begin{cases} \psi_0^{(j)}(\lambda), & \lambda \in [\lambda_0^{(j)}, \lambda_1^{(j)}], \\ \psi_{N_{\lambda_j}+1}^{(j)}(\lambda), & \lambda \in [\lambda_{N_{\lambda_j}-3}^{(j)}, \lambda_{N_{\lambda_j}}^{(j)}], \\ 0, & \text{otherwise.} \end{cases}$$

Because the wind images and the geopotential satisfy different boundary conditions, different basis functions are defined for them. We first define the bicubic spline basis functions $\{\hat{\varphi}_{i,j}\}$ for U and V . Let $\psi_j(\theta) = \frac{1}{4}\bar{\psi}(\frac{\theta+\pi/2}{\Delta\theta} - j + 2)$. We define the one-dimensional cubic spline basis functions that satisfy homogeneous Dirichlet boundary conditions by

$$\begin{aligned}\hat{\beta}_0(\theta) &= \psi_0(\theta) - 4\psi_{-1}(\theta), & \hat{\beta}_1(\theta) &= \psi_1(\theta) - \psi_{-1}(\theta), \\ \hat{\beta}_j(\theta) &= \psi_j(\theta), & j &= 2, \dots, N_\theta - 2, \\ \hat{\beta}_{N_\theta-1}(\theta) &= \psi_{N_\theta-1}(\theta) - \psi_{N_\theta+1}(\theta), & \hat{\beta}_{N_\theta}(\theta) &= \psi_{N_\theta}(\theta) - 4\psi_{N_\theta+1}(\theta).\end{aligned}\quad (12)$$

The bicubic spline basis functions for U and V are defined on \mathcal{S} by

$$\begin{aligned}\hat{\varphi}_{0,0}(\lambda, \theta) &= \hat{\beta}_0(\theta), \\ \hat{\varphi}_{i,j}(\lambda, \theta) &= \beta_i^{(j)}(\lambda)\hat{\beta}_j(\theta), \\ \hat{\varphi}_{0,N_\theta}(\lambda, \theta) &= \hat{\beta}_{N_\theta}(\theta),\end{aligned}\quad (13)$$

for $i = 0, \dots, N_{\lambda_j} - 1$ and $j = 1, \dots, N_\theta - 1$. By construction, the basis functions $\{\hat{\varphi}_{i,j}\}$ are periodic along the longitude and vanish at the poles; that is, they satisfy the boundary conditions (8) for $k = 0, 1$, and 2.

The bicubic spline basis functions for ϕ , denoted by $\{\varphi_{i,j}\}$, are designed to satisfy the boundary conditions (7). Let $m_j(i) \equiv i \bmod N_{\lambda_j}$. The basis functions $\varphi_{i,j}$ are defined on \mathcal{S} by

$$\begin{aligned}\varphi_{0,0}(\lambda, \theta) &= \begin{cases} \psi_0(\theta), & \theta \in [\theta_0, \theta_2], \\ 0, & \text{otherwise,} \end{cases} \\ \varphi_{i,1}(\lambda, \theta) &= \begin{cases} \beta_i^{(1)}(\lambda)\psi_1(\theta), & \lambda \in [\lambda_{m_1(i-2)}^{(1)}, \lambda_{m_1(i+2)}^{(1)}], & \theta \in [\theta_0, \theta_3], \\ \beta_{m_1(k)}^{(1)}(\lambda)\psi_{-1}(\theta), & \lambda \in [\lambda_{m_1(k-2)}^{(1)}, \lambda_{m_1(k+2)}^{(1)}], & \theta \in (\theta_0, \theta_1], \\ 0, & \text{otherwise,} \end{cases} \\ &\quad \text{for } k = i + N_{\lambda_1}/2, \quad i = 0, \dots, N_{\lambda_1} - 1, \\ \varphi_{i,j}(\lambda, \theta) &= \beta_i^{(j)}(\lambda)\psi_j(\theta), \quad \text{for } i = 0, \dots, N_{\lambda_j} - 1, \quad j = 2, \dots, N_\theta - 2, \\ \varphi_{i,N_\theta-1}(\lambda, \theta) &= \begin{cases} \beta_i^{(N_\theta-1)}(\lambda)\psi_{N_\theta-1}(\theta), & \lambda \in [\lambda_{m_{N_\theta-1}(i-2)}^{(N_\theta-1)}, \lambda_{m_{N_\theta-1}(i+2)}^{(N_\theta-1)}], \\ & \theta \in [\theta_{N_\theta-3}, \theta_{N_\theta}], \\ \beta_{m_{N_\theta-1}(k)}^{(N_\theta-1)}(\lambda)\psi_{N_\theta+1}(\theta), & \lambda \in [\lambda_{m_{N_\theta-1}(k-2)}^{(N_\theta-1)}, \lambda_{m_{N_\theta-1}(k+2)}^{(N_\theta-1)}], \\ & \theta \in [\theta_{N_\theta-3}, \theta_{N_\theta}), \\ 0, & \text{otherwise,} \end{cases} \\ &\quad \text{for } k = i + N_{\lambda_{N_\theta-1}}/2, \quad i = 0, \dots, N_{\lambda_{N_\theta-1}} - 1, \\ \varphi_{0,N_\theta}(\lambda, \theta) &= \begin{cases} \psi_{N_\theta}(\theta), & \theta \in [\theta_{N_\theta-2}, \theta_{N_\theta}], \\ 0, & \text{otherwise.} \end{cases}\end{aligned}\quad (14)$$

By construction, the basis functions $\{\varphi_{i,j}\}$ satisfy the boundary conditions (7) for $k=0, 1,$ and 2 . In a finite-difference method discretized on a skipped grid, latitudinal circles with different grid resolutions are often connected by means of spatial interpolation (e.g., [16]). In our method, however, interpolation is done implicitly using the cubic spline representation of the function.

2.2. Discretization of the Shallow Water Equations

To advance the SWE in time, (4)–(6) are first discretized in time using the semi-implicit leapfrog scheme:

$$U^{n+1} + \frac{\Delta t}{R^2} \phi_\lambda^{n+1} = U^{n-1} - \frac{\Delta t}{R^2} \phi_\lambda^{n-1} - 2\Delta t \left(\frac{1}{\cos^2 \theta} (U^n U_\lambda^n + \cos \theta V^n U_\theta^n) - f V^n \right), \quad (15)$$

$$V^{n+1} + \frac{\Delta t}{R^2} \cos \theta \phi_\theta^{n+1} = V^{n-1} - \frac{\Delta t}{R^2} \cos \theta \phi_\theta^{n-1} - 2\Delta t \left(\frac{1}{\cos^2 \theta} (U^n V_\lambda^n + \cos \theta V^n V_\theta^n) + f U^n - \delta^n \right), \quad (16)$$

$$\begin{aligned} \cos \theta \phi^{n+1} + \frac{\Delta t \phi^*}{\cos \theta} (U_\lambda^{n+1} + \cos \theta V_\theta^{n+1}) \\ = \cos \theta \phi^{n-1} - \frac{\Delta t \phi^*}{\cos \theta} (U_\lambda^{n-1} + \cos \theta V_\theta^{n-1}) - \frac{2\Delta t}{\cos \theta} (U^n \phi_\lambda^n + \cos \theta V^n \phi_\theta^n \\ + \phi^n (U_\lambda^n + \cos \theta V_\theta^n)). \end{aligned} \quad (17)$$

Equations (15)–(17) are spatially discretized, and a Helmholtz equation for ϕ^{n+1} is derived from the resulting spatially discretized equations. The Helmholtz equation is derived algebraically rather than analytically (i.e., spatial discretization is done before the Helmholtz equation is derived) in order to preserve the phase velocity of the Rossby waves [17]. To discretize (15)–(17) in space, we approximate the target functions U^{n+1} , V^{n+1} , and ϕ^{n+1} as linear combinations of the bicubic basis functions (13) and (14); that is,

$$U_\Delta^{n+1}(\lambda, \theta) = \sum_{i,j=0}^{N_{\lambda_j}-1, N_\theta} U_{i,j}^{n+1} \hat{\varphi}_{i,j}(\lambda, \theta), \quad (18)$$

$$V_\Delta^{n+1}(\lambda, \theta) = \sum_{i,j=0}^{N_{\lambda_j}-1, N_\theta} V_{i,j}^{n+1} \hat{\varphi}_{i,j}(\lambda, \theta), \quad (19)$$

$$\phi_\Delta^{n+1}(\lambda, \theta) = \sum_{i,j=0}^{N_{\lambda_j}-1, N_\theta} \Phi_{i,j}^{n+1} \varphi_{i,j}(\lambda, \theta). \quad (20)$$

The spline approximations (18)–(20) are substituted into (15)–(17) and the spline coefficients $U_{i,j}^{n+1}$, $V_{i,j}^{n+1}$, and $\Phi_{i,j}^{n+1}$ are determined by imposing the collocation conditions at the appropriate collocation points. Normally, the collocation points for a cubic spline collocation method are the grid points, that is, the set \mathcal{S} . However, in this implementation, the poles ($\theta = \pm\pi/2$), which are included in \mathcal{S} , are not chosen to be collocation points for

the following reasons. As ϕ_λ^{n+1} vanishes at the poles, (15) and (16) reduce to the latitudinal boundary conditions for U^{n+1} and V^{n+1} ,

$$U^{n+1}(\lambda, \pm\pi/2) = 0, \quad V^{n+1}(\lambda, \pm\pi/2) = 0,$$

respectively, thus giving rise to an insufficient number of conditions for determining the spline approximations (18)–(20). Moreover, although the term $U_\lambda^{n+1}/\cos\theta$ in (17) is bounded at the poles, its value cannot be computed from the spline representation of U^{n+1} . Thus, we choose the collocation points to be

$$\Gamma \equiv \{\tau_{i,j} \equiv (\lambda_i^{(j)}, \theta_j)\}_{i=0, j=1}^{N_\lambda-1, N_\theta-1} \cup \{\tau_{0,0} \equiv (0, -\pi/2 + \Delta\theta/2), \tau_{0, N_\theta} \equiv (0, \pi/2 - \Delta\theta/2)\}.$$

Substituting (18)–(20) into (15)–(17) and imposing the collocation conditions at Γ , we obtain

$$\begin{aligned} & U_\Delta^{n+1}(\tau_{i,j}) + \frac{\Delta t}{R^2} D_\lambda \phi_\Delta^{n+1}(\tau_{i,j}) \\ &= U_\Delta^{n-1}(\tau_{i,j}) - \frac{\Delta t}{R^2} D_\lambda \phi_\Delta^{n-1}(\tau_{i,j}) - 2\Delta t \left(\frac{1}{\cos^2 \theta_j} (U_\Delta^n(\tau_{i,j}) D_\lambda U_\Delta^n(\tau_{i,j}) \right. \\ &\quad \left. + \cos \theta_j V_\Delta^n(\tau_{i,j}) D_\theta U_\Delta^n(\tau_{i,j})) - f V_\Delta^n(\tau_{i,j}) \right) \\ &\equiv R_u^n(\tau_{i,j}), \end{aligned} \tag{21}$$

$$\begin{aligned} & V_\Delta^{n+1}(\tau_{i,j}) + \frac{\Delta t}{R^2} \cos \theta_j D_\theta \phi_\Delta^{n+1}(\tau_{i,j}) \\ &= V_\Delta^{n-1}(\tau_{i,j}) - \frac{\Delta t}{R^2} \cos \theta_j D_\theta \phi_\Delta^{n-1}(\tau_{i,j}) - 2\Delta t \left(\frac{1}{\cos^2 \theta_j} (U_\Delta^n(\tau_{i,j}) D_\lambda V_\Delta^n(\tau_{i,j}) \right. \\ &\quad \left. + \cos \theta_j V_\Delta^n(\tau_{i,j}) D_\theta V_\Delta^n(\tau_{i,j})) + f U_\Delta^n(\tau_{i,j}) - \delta_\Delta^n(\tau_{i,j}) \right) \\ &\equiv R_v^n(\tau_{i,j}), \end{aligned} \tag{22}$$

$$\begin{aligned} & \cos \theta_j \phi_\Delta^{n+1}(\tau_{i,j}) + \frac{\Delta t \phi^*}{\cos \theta_j} (D_\lambda U_\Delta^{n+1}(\tau_{i,j}) + \cos \theta_j D_\theta V_\Delta^{n+1}(\tau_{i,j})) \\ &= \cos \theta_j \phi_\Delta^{n-1}(\tau_{i,j}) - \frac{\Delta t \phi^*}{\cos \theta_j} (D_\lambda U_\Delta^{n-1}(\tau_{i,j}) + \cos \theta_j D_\theta V_\Delta^{n-1}(\tau_{i,j})) \\ &\quad - \frac{2\Delta t}{\cos \theta_j} (U_\Delta^n(\tau_{i,j}) D_\lambda \phi_\Delta^n(\tau_{i,j}) + \cos \theta_j V_\Delta^n(\tau_{i,j}) D_\theta \phi_\Delta^n(\tau_{i,j})) \\ &\quad + \phi^n (D_\lambda U_\Delta^n(\tau_{i,j}) + \cos \theta_j D_\theta V_\Delta^n(\tau_{i,j})) \\ &\equiv R_\phi^n(\tau_{i,j}), \end{aligned} \tag{23}$$

where $\delta_\Delta^n \equiv (U_\Delta^{n2} + V_\Delta^{n2}) \sin \theta / \cos^2 \theta$.

To solve (21)–(23), the divergence terms are eliminated from the discretized continuity equation (23) using (21) and (22) to yield a Helmholtz equation. To this end, let bold typeface denote vectors. For example, Φ_Δ^{n+1} denotes the vector $(\phi_\Delta^{n+1}(\tau_{i,j}))_{i=0, j=0}^{N_\lambda-1, N_\theta}$, arranged in a natural ordering; that is, $(\Phi_\Delta^{n+1})_k = \phi_\Delta^{n+1}(\tau_{i,j})$, where $k = i + \sum_{l=0}^{j-1} N_\lambda$. Let \hat{M} and M

denote the mass matrix associated with the basis functions (13) and (14), respectively; that is,

$$M_{m,n} = \psi_{i,j}(\tau_{k,l}), \quad \hat{M}_{m,n} = \hat{\psi}_{i,j}(\tau_{k,l}), \quad (24)$$

where $m = k + \sum_{s=0}^{s=l-1} N_{\lambda_s}$ and $n = i + \sum_{s=0}^{s=j-1} N_{\lambda_s}$. By eliminating the divergence terms from the continuity equation (23), we obtain the discrete Helmholtz equation

$$\begin{aligned} \cos \theta_j \Phi_{\Delta}^{n+1} - \left(\frac{\Delta t}{R} \right)^2 \frac{\phi^*}{\cos \theta_j} (D_{\lambda} \hat{M}^{-1} D_{\lambda} + \cos \theta_j D_{\theta} \hat{M}^{-1} (\cos \theta_j D_{\theta})) \Phi_{\Delta}^{n+1} \\ = \mathbf{R}_{\phi}^n - \frac{\Delta t \phi^*}{\cos \theta_j} (D_{\lambda} \hat{M}^{-1} \mathbf{R}_u^n + \cos \theta_j D_{\theta} \hat{M}^{-1} \mathbf{R}_v^n). \end{aligned} \quad (25)$$

Equation (25) is solved using the conjugate gradient method. Once Φ_{Δ}^{n+1} is computed, $\mathbf{U}_{\Delta}^{n+1}$ and $\mathbf{V}_{\Delta}^{n+1}$ are updated using (21) and (22).

3. NUMERICAL RESULTS

We applied the cubic spline collocation method to the complete Williamson *et al.* test suite for the SWE in spherical geometry [19]. In this section, we present convergence results for test cases 1, 2, and 4, for which analytic solutions exist, and for test case 5. We note that the method also generated stable and convergent numerical solutions for the other test cases (3, 6, and 7). For a detailed description of the test cases, we refer the reader to [19]. We then compare efficiency of the method developed in Section 2 to the efficiency of a similar method with the bicubic spline basis functions defined on a uniform grid. All computations reported below were performed using Fortran programs in double precision on a Dell system with a 700-MHz Pentium III processor and 128-MB RAM.

3.1. Convergence Results

Test Case 1 (Advection of Cosine Bell over the Pole)

The first test case in the suite tests the advective component of the numerical method in isolation. A cosine bell was advected once around the sphere. The orientation of the advecting wind is determined by the parameter α , which is the angle between the axis of solid body rotation and the polar axis of the spherical coordinate system. Advecting winds with different orientations were simulated, including advection around the equator ($\alpha = 0$), directly over the poles ($\alpha = \pi/2$), and with minor shifts from these two orientations ($\alpha = 0.05$ and $\pi/2 - 0.05$). A time step of $\Delta t = 30$ min was used in all simulations. Table I contains

TABLE I
Convergence Results Test Case 1 with $\alpha = \pi/2$ after 12 Days

N_{θ}	$l_1(\phi)$	Rate	$l_2(\phi)$	Rate	$l_{\infty}(\phi)$	Rate
16	1.0898E-1	—	1.5966E-1	—	3.0899E-1	—
32	5.1729E-2	1.08	7.8566E-2	1.02	1.4118E-1	1.13
64	2.6225E-2	0.98	4.0053E-2	0.97	7.1033E-2	0.99
128	1.3388E-2	0.97	2.0166E-2	0.99	3.6012E-2	0.98

TABLE II
Convergence Results for Test Case 2 with $\alpha = 0$ after 5 Days

N_θ	$l_1(\phi)$	Rate	$l_2(\phi)$	Rate	$l_\infty(\phi)$	Rate
16	1.7964E-5	—	2.5216E-5	—	4.9508E-5	—
32	1.2117E-6	3.89	1.5543E-6	4.02	2.8276E-6	4.13
64	7.8404E-8	3.95	9.9183E-8	3.97	1.7919E-7	3.98
128	5.8822E-9	3.74	7.0227E-9	3.82	1.2341E-9	3.86

normalized global errors in ϕ after 12 days for $\alpha = \pi/2$ for successively refined spatial resolutions. The definitions for the L_1 -, L_2 -, and L_∞ -error norms, denoted by l_1 , l_2 , and l_∞ , respectively, can be found in [19]. In most of the simulations (except for $N_\theta = 16$), solutions translated with little change in shape. However, because the second derivatives in the initial data are discontinuous, solutions for case 1 show only first-order convergence in space.

Test Case 2 (Global Steady State Nonlinear Zonal Geostrophic Flow)

This case is a steady state solution to the nonlinear SWE. It consists of solid body rotation or zonal flow with the corresponding geostrophic height field. The wind velocity and geopotential are initially (and for all time) given by

$$u = u_0(\cos \theta \cos \alpha + \cos \lambda \sin \theta \sin \alpha), \quad (26)$$

$$v = -u_0 \sin \lambda \sin \alpha, \quad (27)$$

$$\phi = \phi_0 - \left(R\Omega u_0 + \frac{u_0^2}{2} \right) (-\cos \lambda \cos \theta \sin \alpha + \sin \theta \cos \alpha)^2, \quad (28)$$

where $u_0 = 2\pi R/(12 \text{ days})$, $\phi_0 = 2.94 \times 10^4 \text{ m}^2/\text{s}^2$, and α , as in test case 1, is the angle between the axis of solid body rotation and the polar axis of the spherical coordinate system.

A time step of $\Delta t = 30 \text{ min}$ was used. Tables II and III show normalized global errors in ϕ after 5 days for $\alpha = 0$ and $\pi/2$, respectively, for successively refined spatial resolutions. Fourth-order convergence was observed with $\alpha = 0$, but third-order convergence was obtained for $\alpha = \pi/2$ and for other nonzero α values (e.g., $\pi/4$, results not shown). Similar convergence results were also obtained for U and V .

Cubic spline interpolants exhibit fourth-order superconvergence at grid points [5, 9, 14], and the cubic spline collocation method yields fourth-order approximations for a first-order differential problem. In this implementation, spatial discretization is done on the first-order system (15)–(17) before the divergence terms are eliminated, in order for the method to

TABLE III
Convergence Results for Test Case 2 with $\alpha = \pi/2$ after 5 Days

N_θ	$l_1(\phi)$	Rate	$l_2(\phi)$	Rate	$l_\infty(\phi)$	Rate
16	1.6517E-5	—	2.0901E-5	—	4.2503E-5	—
32	2.0362E-6	3.02	2.5236E-6	3.05	4.9571E-6	3.10
64	2.6534E-7	2.94	3.0470E-7	3.01	5.7415E-7	2.95
128	3.6295E-8	2.87	3.9158E-8	2.96	7.4300E-8	2.95

be neutrally stable for the Rossby waves [17]. As a results, the Helmholtz equation (25) is actually a pseudo-Helmholtz equation, in the sense that the second derivatives of ϕ_{Δ}^{n+1} are approximated by applying the first derivative operators twice. Thus, one may expect the numerical solutions obtained using the cubic spline collocation method to exhibit fourth-order convergence. This is indeed the case for $\alpha = 0$, in which the geopotential is given by

$$\phi = \phi_0 - \left(R\Omega u_0 + \frac{u_0^2}{2} \right) \sin^2 \theta. \tag{29}$$

However, only third-order convergence was obtained for $\alpha = \pi/2$. In this case, the geopotential is given by

$$\phi = \phi_0 - \left(R\Omega u_0 + \frac{u_0^2}{2} \right) (\cos \lambda \cos \theta)^2. \tag{30}$$

At the beginning of the simulation with $\alpha = \pi/2$, large errors were observed near the poles. In fact, the errors in a short simulation (about a day) were fourth order except near the poles; close to the poles, the errors were found to be third order. We attribute this suboptimal convergence (i.e., a convergence that is less than fourth order) to the $1/\cos \theta$ terms in the Helmholtz equation (25). These terms become $\mathcal{O}(1/\Delta\theta)$ as θ approaches $\pm\pi/2$, giving rise to larger truncation errors and reducing the order of convergence by one near the poles. As the stimulation progressed, these larger errors propagated over the sphere and eventually contaminated the rest of the solution. The phenomenon has been reported elsewhere [18].

Suboptimal convergence was not observed in the case of $\alpha = 0$ for the following reasons. The $1/\cos \theta$ terms in (25) are associated with the λ derivative of ϕ_{Δ}^{n+1} and with R_u^n . It follows from (29) that $D_{\lambda}\phi_{\Delta}^{n+1} \approx 0$. Moreover, every term in R_u^n is either approximately zero (e.g., $D_{\lambda}\phi_{\Delta}^{n-1}$) or is scaled by $\cos \theta$ (e.g., U_{Δ}^n and V_{Δ}^n). Therefore, the errors remained fourth order even close to the poles.

Test Case 4 (Forced Nonlinear System with a Translating Low)

In this test case forcing terms are added to the right sides of (4)–(6) so that analytic solutions are known a priori for the resulting nonlinear unsteady equations. A time step of $\Delta t = 15$ min was used. Table IV shows normalized global errors in ϕ after 5 days for different spatial resolutions. In this test, the activities of the geopotential as well as the wind velocities are limited to regions that are relatively far away from the poles (the center of the low is initially located at $(0, \pi/4)$). As a results, fourth-order spatial convergence was obtained for ϕ (see Table IV) and also for U and V (results not shown).

TABLE IV
Convergence Results for Test Case 4

N_{θ}	$l_1(\phi)$	Rate	$l_2(\phi)$	Rate	$l_{\infty}(\phi)$	Rate
16	3.3350E-4	—	7.1577E-4	—	6.1468E-3	—
32	2.0700E-5	4.01	4.0598E-5	4.14	3.7627E-4	4.03
64	1.4157E-6	3.87	2.6087E-6	3.96	4.1572E-5	3.25
128	9.5412E-8	3.89	1.7842E-7	3.87	2.3744E-6	4.13

Test Case 5 (Zonal Flow over an Isolated Mountain)

Test case 5 consists of zonal flow as in case 2, with $\alpha = 0$, impinging on a mountain. Because the analytic solution is not known for this case, we compared our results to highly refined spectral transform solutions [12]. As in the reference solution, explicit diffusion was used to maintain numerical stability. At each time step, we applied to the prognostic variables the scale- and resolution-dependent filter

$$\xi^n \leftarrow \xi^n - c \Delta \lambda^4 \nabla^4 \xi^n, \quad (31)$$

where $\xi = \phi, U, \text{ or } V$, and $c = 10^{-4} R^4$. By scaling the diffusion term by $\Delta \lambda^4$, we ensure that the discrepancy introduced by the explicit diffusion to the numerical solution is of the same order as the spatial truncation error and, as a result, does not affect the spatial convergence rate. Explicit diffusion was also used in our simulations of cases 6 and 7.

A time step of $\Delta t = 15$ min was used. Figure 2 shows the evolution of normalized L_2 -error in ϕ , computed on successively refined spatial resolutions, for 15 days. The numerical solutions were stable but errors failed to converge to zero for two reasons. First, the zonal flow initial conditions and the topography are not in geostrophic balance. Thus, gravity waves of significant magnitude are generated; these waves are poorly resolved by the semi-implicit reference solution (and by our solution), resulting in an uncertainty of approximately 10^{-3} in the normalized L_∞ geopotential error. Furthermore, the orography has a discontinuous first derivative and thus violates the smoothness assumption in the cubic spline expansion. Despite these difficulties, our method, coupled with explicit damping, was stable and produced convergent approximations. Indeed, for resolutions higher than $N_\theta = 64$, the normalized geopotential error remains approximately 10^{-3} for 15 days.

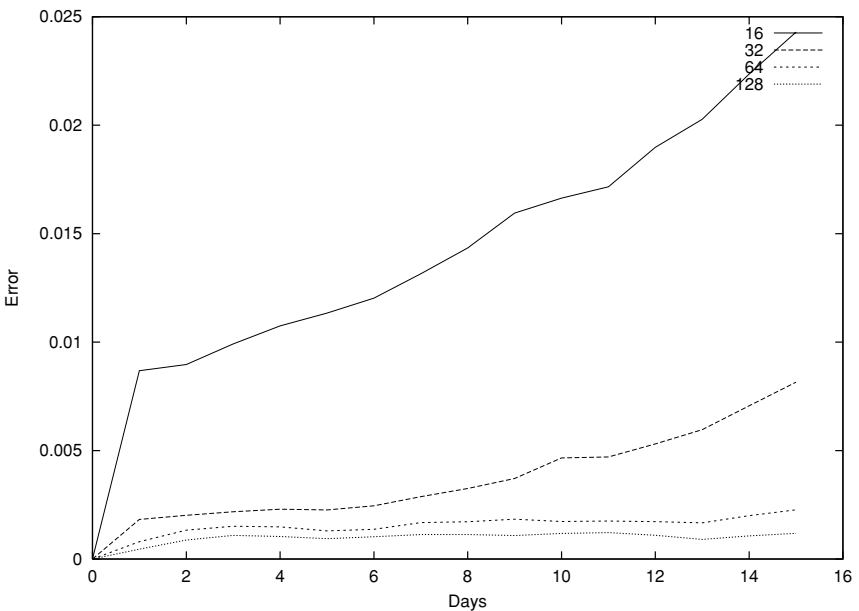


FIG. 2. Evolution of normalized l_2 geopotential error for test case 5 for 15 days.

3.2. Efficiency Results

In this section, we compare the cubic spline collocation method developed in Section 2 to a similar method derived on a uniform latitude–longitude grid. We refer to these two methods as the skipped-grid formulation and the uniform-grid formulation, respectively, of the cubic spline collocation method.

On a uniform grid, N_{λ_j} , the number of grid points along the j th latitude circle, is given by

$$N_{\lambda_j} = \begin{cases} 0, & j = 0, N_\theta, \\ 2N_\theta, & 0 < j < N_\theta. \end{cases} \quad (32)$$

The bicubic spline basis functions, $\{\hat{\phi}_{i,j}\}$ and $\{\varphi_{i,j}\}$, for the uniform-grid formulation are given by (13) and (14), respectively.

Test case 2 with $\alpha = \pi/2$ is used in the efficiency study. Figure 3 shows the L_2 -errors for the geopotential, after 5 days, versus total computational time in seconds for the two formulations, in a log–log plot, for $N_\theta = 16, 32, 64,$ and 128 . The curve for the skipped-grid formulation has a slope of approximately -1.5 ; the curve for the uniform-grid formulation has a similar slope at low resolutions, but the slope becomes less negative at high resolutions, which implies a reduction in efficiency.

A time step Δt of 30 min was used in all simulations for the skipped-grid formulation. As the spatial resolution increased, the errors decreased at a rate of approximately $\mathcal{O}(\Delta\theta^3)$ (see Table III). Because the cubic splines give rise to sparse matrices with $\mathcal{O}(N_\theta^2)$ entries, provided that the number of the conjugate gradient iterations remains approximately constant as N_θ

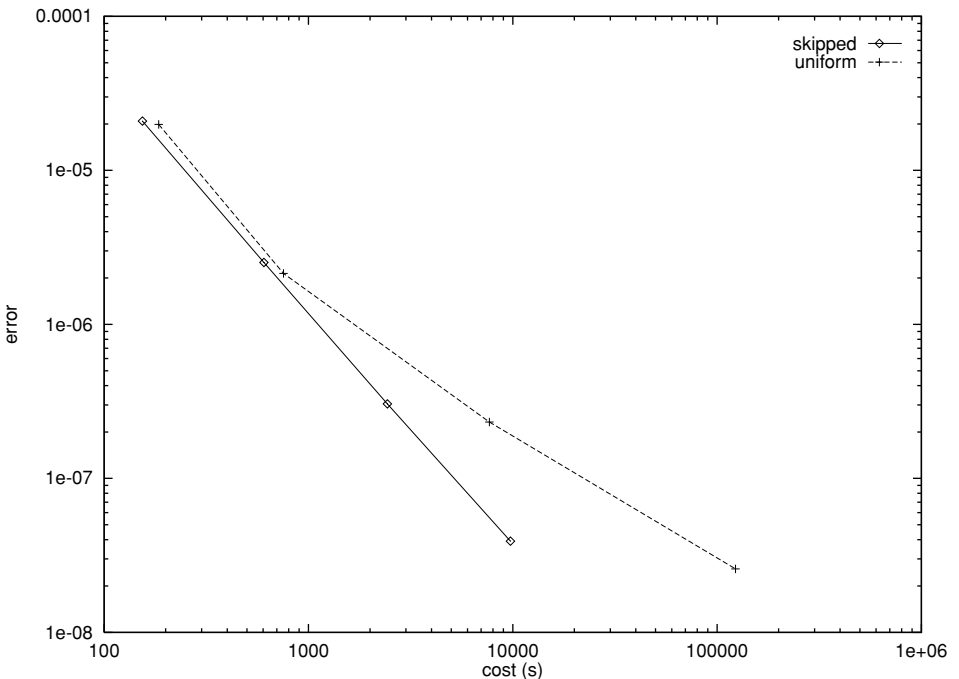


FIG. 3. Efficiency results for skipped-grid and uniform-grid formulations.

increases, the total work in the method should increase by about a factor of four as N_θ is doubled. Indeed, our results show that the computation cost of the skipped-grid formulation increases approximately quadratically.

The uniform-grid formulation gives rise to more accurate solutions: $l_2(\phi) = 1.9872 \times 10^{-5}$, 2.1414×10^{-6} , 2.3327×10^{-7} , and 2.5832×10^{-8} for $N_\theta = 16, 32, 64,$ and 128 , respectively. However, the uniform-grid formulation is also more expensive, since the uniform grid has approximately 25% more grid points than the skipped grid for the same N_θ . Consequently, the uniform-grid formulation is slightly less efficient than the skipped-grid formulation for this problem at low resolutions ($N_\theta = 16$ and 32). As the spatial grid is refined, the efficiency of the uniform-grid formulation deteriorates (the slope of its error-cost curve in Fig. 3 becomes less negative). This is because at higher resolutions ($N_\theta \geq 64$), a smaller time step is required to maintain numerical stability owing to the CFL condition. Specifically, a time step of 30 min, which is the same as that used for the skipped-grid formulation, was used for $N_\theta = 16$ and 32 . At $N_\theta = 64$, the CFL restriction reduced the time step to 12 min, and the time step was further reduced to 3 min at $N_\theta = 128$. Thus, for $N_\theta \geq 64$, the computation cost of the uniform-grid formulation increases as $\mathcal{O}(N_\theta^4)$. We therefore conclude that for this problem the skipped-grid formulation is more efficient than the uniform-grid formulation.

In the above comparison, the same time step is used for all spatial resolutions for the skipped-grid formulation and is reduced for high resolutions ($N_\theta \geq 64$) for the uniform formulation. If the maximum time step allowed by the CFL condition is used, then the computational complexities for the skipped-grid and uniform formulations can be shown to be $\mathcal{O}(N_\theta^3)$ and $\mathcal{O}(N_\theta^4)$, respectively. In this case, the computational complexity of the skipped-grid formulation is still lower than that of the uniform-grid formulation.

4. DISCUSSION AND SUMMARY

In most global meteorological applications, spatial discretization schemes are based on spectral methods [11, 21] or low-order finite-difference/finite-element methods [3, 13]. Spectral methods yield high-order solutions and the spectral transform method gives rise to elliptic equations that are computationally inexpensive to solve. However, spectral methods also give rise to dense matrices and the spectral transform method requires Legendre transforms, which have a computational complexity of $\mathcal{O}(N^3)$. On the other hand, finite-element methods may have a computational complexity of $\mathcal{O}(N^2)$; these methods also have more potential for parallelism and give rise to reasonably scalable parallel implementations. Therefore, high-order finite-element methods seem to be a viable alternative to the spectral transform method.

In this paper, we present a numerical method that combines the semi-implicit leapfrog scheme and the cubic spline collocation method for solving the SWE on the sphere. Discretization is done on a skipped latitude–longitude grid, and bicubic spline basis functions are constructed to satisfy the boundary conditions imposed on the target functions. Numerical results for the standard SWE test cases [19] are presented to demonstrate the stability and accuracy of the method. In particular, the poles do not introduce any numerical instability. The method gives rise to numerical approximations that are third order near the poles and fourth order elsewhere. We also show that the method has a computational cost of $\mathcal{O}(N^2)$ and that the skipped-grid formulation is more efficient than the uniform-grid formulation.

ACKNOWLEDGMENT

I thank Dr. Steve Thomas of the National Center for Atmospheric Research for a careful reading of this manuscript and for his insightful comments.

REFERENCES

1. J. Côté, J.-G. Desmarais, S. Gravel, A. Méthot, A. Patoine, M. Roch, and A. Staniforth, The operational CMC-MRB global environment multiscale (GEM) model. Part II: Results, *Mon. Weather Rev.* **126**, 1397 (1998).
2. J. Côté, S. Gravel, A. Méthot, A. Patoine, M. Roch, and A. Staniforth, The operational CMC-MRB global environmental multiscale (GEM) model. Part I: Design considerations and formulation, *Mon. Weather Rev.* **126**, 1373 (1998).
3. J. Côté, M. Roch, A. Staniforth, and L. Fillion, A variable-resolution semi-Lagrangian finite-element global model of the shallow-water equations, *Mon. Weather Rev.* **121**(1), 231 (1993).
4. J. Côté and A. Staniforth, An accurate and efficient finite-element global model of the shallow water equations, *Mon. Weather Rev.* **118**, 2707 (1990).
5. C. de Boor, On the convergence of odd degree spline interpolation, *J. Approx. Theory* **1**, 452 (1968).
6. C. de Boor, *A Practical Guide to Splines* (Springer-Verlag, New York, 1978).
7. W. L. Gates and C. A. Riegel, A study of numerical errors in the integration of barotropic flow on a spherical grid, *J. Geophys. Res.* **67**(2), 773 (1962).
8. J. Göttelmann, A spline collocation scheme for the spherical shallow water equations, *J. Comput. Phys.* **148**, 297 (1999), doi:jcph.1998.6111.
9. C. A. Hall, On error bounds for spline interpolation, *J. Approx. Theory* **1**, 209 (1968).
10. G. J. Haltiner and R. T. Williams, *Numerical Prediction and Dynamic Meteorology* (Wiley, New York, 1980).
11. M. Hortal, Aspects of numerics of the ECMWF model, in *Proceedings of a Seminar Held at ECMWF on Recent Developments in Numerical Methods for Atmospheric Modeling, 1999* (European Centre for Medium-Range Weather Forecasts, Reading, UK, 1999).
12. R. Jakob, J. J. Hack, and D. L. Williamson, *Solutions to the Shallow Water Test Set Using the Spectral Transform Method*, Technical Report NCAR/TN-388+STR (National Center for Atmospheric Research, 1993).
13. Y. Kurihara, Numerical integration of the primitive equations on a spherical grid, *Mon. Weather Rev.* **93**(7), 399 (1965).
14. T. R. Lucas, Error bounds for interpolating cubic splines under various end conditions, *SIAM J. Numer. Anal.* **11**, 569 (1974).
15. P. M. Prenter, *Splines and Variational Methods* (Wiley, New York, 1989).
16. R. J. Purse, Accurate numerical differencing near a polar singularity of a skipped grid, *Mon. Weather Rev.* **116**, 1067 (1988).
17. A. Staniforth and H. Mitchell, A semi-implicit finite-element barotropic model, *Mon. Weather Rev.* **105**, 154 (1977).
18. D. L. Williamson and G. L. Browning, Comparison of grids and difference approximations for numerical weather prediction over a sphere, *J. Appl. Meteorol.* **12**, 264 (1973).
19. D. L. Williamson, J. B. Drake, J. J. Hack, R. Jakob, and P. N. Swarztrauber, A standard test set for numerical approximations to the shallow water equations in spherical geometry, *J. Comput. Phys.* **102**, 211 (1992).
20. D. L. Williamson and R. Laprise, Numerical approximations for global atmospheric general circulation models, in *Numerical Modelling of the Global Atmosphere in the Climate System*, edited by P. Mote and A. O'Neill, NATO Science Series, p. 127. (2000).
21. D. L. Williamson and J. G. Olson, Climate simulations with a semi-Lagrangian version of the NCAR community climate model, *Mon. Weather Rev.* **122**, 1594 (1993).